ACS Photonics

pubs.acs.org/journal/apchd5

Article

Defect-Enhanced Exciton−Exciton Annihilation in Monolayer Transition Metal Dichalcogenides at High Exciton Densities

Tianju Zhang and Jun Wang*

Cite This: https://doi.org/10.1021/acsphotonics.1c00932

Read Online

ACCESS | Metrics & More | Article Recommendations | Supporting Information

ABSTRACT: The exciton−exciton annihilation (EEA) process easily occurs in monolayer transition metal dichalcogenides (TMDs) because of the strong Coulomb interaction and quantum confinement effect, which enhance the many-body interaction of excitons. This process can affect the performance of the optoelectronic devices. It is crucial to examine the effect of defect states on the EEA process and determine whether it is comparable to that at the low excitation intensities, particularly when applied to laser devices at a high exciton density. In this study, femtosecond transient absorption spectroscopy was used to explore the EEA process of four types of CVD-grown monolayer TMDs (i.e., WS_2, WSe_2, MoS_2, and $MoSe_2$). We demonstrated that the defect-assisted EEA process of local excitons is enhanced and plays a key role in the exciton relaxation process at high exciton densities of approximately 10^{12} cm^{-2} below a Mott density of approximately 10^{13} cm^{-2}. The measured EEA rates for WS_2, WSe_2, $MoSe_2$, and MoS_2 were 0.016, 0.026, 0.049, and 0.102 cm^2/s, respectively, implying that EEA is enhanced as defect states increase in monolayer TMDs. Our results provide a profound insight into the effect of defect states on the EEA process in monolayer TMDs at high exciton densities.

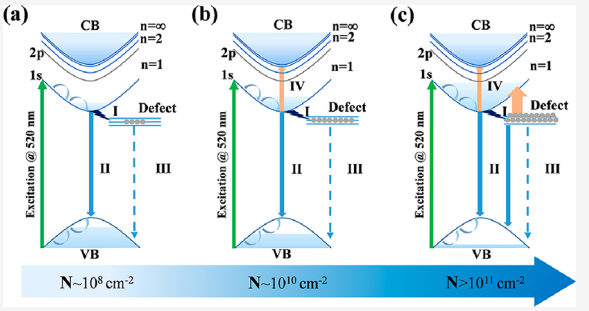

KEYWORDS: *defect states, monomolecular recombination, two-body recombination, exciton saturation density, femtosecond transient absorption spectroscopy*

Two-dimensional (2D) layered transition metal dichalcogenides (TMDs) with the chemical structure of MX_2 (M: Mo or W; X: S, Se, or Te) have garnered significant interest in the past decade owing to their many unique optical and electronic properties, such as layer-dependent bandgap, high electron mobility, high third-order nonlinear polarizability and susceptibility, and spin−valley interactions.[1−9] Compared to multilayer TMDs, the bandgap in monolayer TMDs becomes a direct bandgap in the visible to near-IR region, and the exciton binding energy in the material increases to approximately 300 meV.[10−12] The reason is that the dielectric screening effect of the exciton is weakened and the spatial confinement effect of the wave function is enhanced.[13−16] The enhanced stability of the excitons in monolayer materials not only improves the photoluminescence quantum yield (PLQY) at room temperature, making these materials efficient light emitters and single-photon sources[1,11,17] but also provides an opportunity to study the steady-state and dynamic physical properties of excitons to explore new applications,[14−16,18−28] such as field-effect transistors and ultrasensitive photodetectors.[29−34]

The exciton dynamics can be highly modulated by the electron−hole density generated by the optical carrier injection of ultrashort laser pulses and electrical tuning.[19,35] This is primarily attributed to the competition of various physical processes of exciton relaxation, namely, first-order recombination (such as exciton radiation recombination and defect-assisted nonradiation recombination) and bimolecular recombinations.[14,19−22,24−26,35,36] The reduced dimensional systems can enhance the many-body interaction of excitons, such that at higher carrier densities, the physical process of exciton−exciton annihilation (EEA) becomes extremely effective and dominant in the exciton dynamics and significantly reduces the PLQY.[22,37−39] The main reason is that EEA is a scattering mechanism in which one exciton nonradiation recombination transfers its energy and momentum to another exciton excited to a higher energy state, and the former exciton subsequently relaxes to a lower energy state and loses the originally obtained energy through electron−phonon interaction.[40−43] In general, EEA can occur through two different mechanisms: a direct Förster resonance energy transfer (FRET) and multistep diffusion.[44,45] For A and B excitons in 2D TMDs, the dipole−dipole interaction is enhanced by the overlap between the absorption spectrum and the emission spectrum of the exciton state, causing EEA by the FRET process, while the EEA of C

Received: June 22, 2021

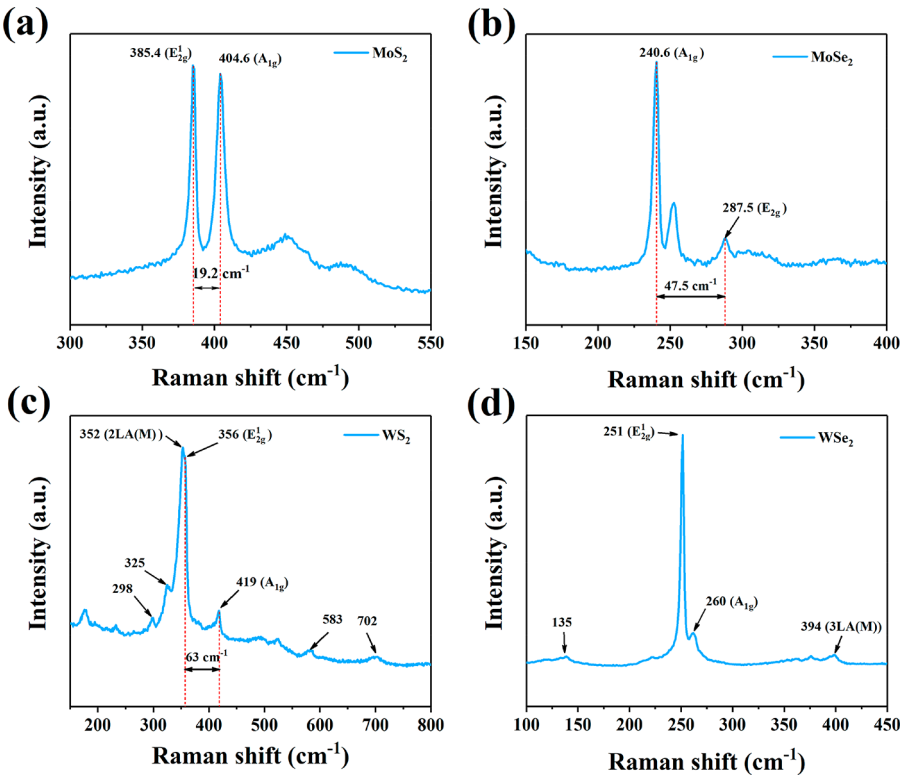

Figure 1. Raman spectra results of the four monolayer CVD-grown materials: (a) MoS_2, (b) $MoSe_2$, (c)WS_2, and (d) WSe_2.

exciton is caused by the diffusion mechanism.[45] Although EEA rates of TMDs have been explored, EEA rates for a particular material obtained in different studies are quite different because of the differences in sample preparation methods and experimental test conditions.[22,38,39,46−49] For example, Huang et al. determined the EEA rate of mechanically stripped monolayer WS_2 as 0.41 ± 0.02 cm^2/s using time-resolved photoluminescence spectroscopy, whereas Jonker et al. calculated the EEA rate of chemical vapor deposition (CVD)-grown monolayer WS_2 as 0.089 ± 0.001 cm^2/s using ultrafast transient absorption spectroscopy.[22,39] The difference in the density of defect states in the test samples may be one of the factors causing this inconsistency, mainly as the experimental results and theoretical calculations have shown that the defect can annihilate the exciton by Auger recombination.[20,50] The exciton relaxation processes related to defect states depend on the exciton concentration. When exciton densities are in the low and medium densities of approximately 10^{10} cm^{-2}, the defect states can capture the excitons and weaken the EEA process.[39,46] However, at high exciton densities below a Mott density of approximately 10^{13} cm^{-2}, the effect of defect states on the EEA process has not been examined thoroughly.

For the 2H phase of monolayer TMDs with a similar band structure, the chemical structure of MX_2 (M: Mo or W; X: S, Se, or Te) arranged into the hexagonal honeycomb network, possess a direct bandgap, in which the minimum value of conduction band and the maximum value of valence band are located at the binary indexed corners K^+ and K^- of the 2D hexagonal Brillouin zone.[51,52] The major orbital contribution at the valence band edge is the $d_{x^2-y^2}$ and d_{xy} orbitals of the metal M, which hybridize with p_x and p_y orbitals of the chalcogen X. As for the conduction band edge, it is dominated by the $d_{3z^2-r^2}$ orbital of M and the p_x and p_y orbitals of X.[52] Besides, the most common atomic defects are chalcogen-atom vacancies in monolayer TMDs, in which chalcogen-atom vacancies tend to remain isolated in WS_2 films and form hybridized vacancy chains in the MoS_2, $MoSe_2$, and WSe_2 films.[53] So the EEA rates of four CVD-grown monolayer TMDs (WS_2, WSe_2, MoS_2, and $MoSe_2$) having different densities of defect states almost up to 10^{12} cm^{-2} have not been compared under the identical experimental conditions to further clarify the effect of different defect states on EEA rates. Moreover, the CVD method can grow large-area monolayer TMDs to realize the wide application of TMDs in semiconductor manufacturing lines.[54]

In this study, we used femtosecond transient absorption (TA) spectroscopy to investigate the EEA process of four CVD-grown monolayer TMDs (i.e., WS_2, WSe_2, MoS_2, and $MoSe_2$) at high exciton densities of ~10^{12} cm^{-2} below a Mott density of ~10^{13} cm^{-2}. The four CVD-grown materials were proved to be monolayer ones using steady-state Raman spectroscopy, atomic force microscopy (AFM), and photoluminescence (PL) spectroscopy. The results of TA spectroscopy demonstrate that the defect-assisted EEA process of local excitons is enhanced and plays a key role in the exciton relaxation process when the exciton density exceeds a value of approximately 10^{12} cm^{-2} due to the defect localized effect. The measured EEA rates for the atomically thin-layered WS_2, WSe_2, $MoSe_2$, and MoS_2 were 0.016, 0.026, 0.049, and 0.102 cm^2/s, respectively, implying that EEA is enhanced as the defect states increase in monolayer TMDs. These results help determine the effect of the defect states on the EEA process in monolayer TMDs at high exciton densities and optimize advanced light-emitting devices based on monolayer TMDs.

CVD-grown monolayer TMDs (i.e., WS_2, WSe_2, MoS_2, and $MoSe_2$) prepared on a sapphire substrate supported by Six Carbon Technology Shenzhen were confirmed to be

https://doi.org/10.1021/acsphotonics.1c00932
ACS Photonics XXXX, XXX, XXX−XXX

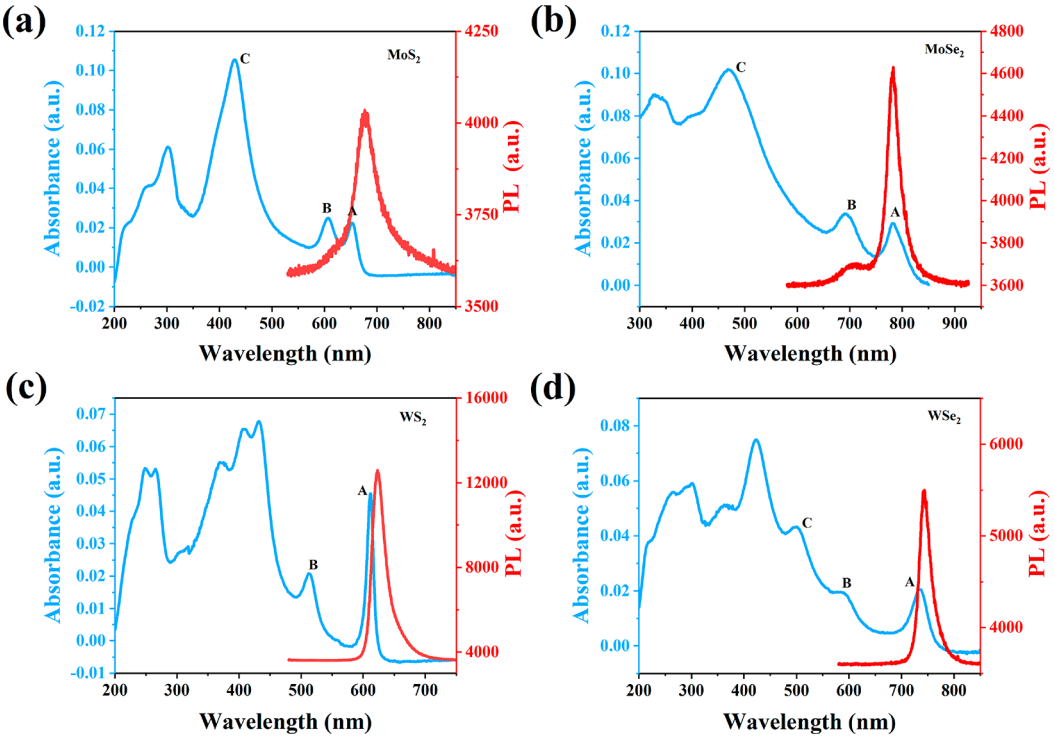

Figure 2. Absorption (the light blue solid line) and PL spectra (the red solid line) of the four monolayer CVD-grown materials: (a) MoS_2, (b) $MoSe_2$, (c)WS_2, and (d) WSe_2.

monolayer using Raman spectroscopy, AFM, and PL spectroscopy, whose homogeneity is demonstrated by using the optical microscope images and Raman mapping, as shown in Figure S1. A systematic investigation on the Raman vibrational properties of monolayer MoS_2, WS_2, WSe_2, and $MoSe_2$ was performed at room temperature using a continuous wave (CW) laser with a wavelength of 532 nm, as shown in Figure 1. The Raman spectra of MoS_2 shows a strong in-plane mode E_{2g}^1 (385.4 cm^{-1}) and out-of-plane mode A_{1g} (404.6 cm^{-1}) with a difference of 19.2 cm^{-1}, which proves that the MoS_2 film is a monolayer material.[4,55] As for $MoSe_2$, the most obvious Raman mode A_{1g} (240.6 cm^{-1}) related to the out-of-plane vibration of the Se atom and weak Raman mode E_{2g}^1 (287.5 cm^{-1}) related to the in-plane vibration of the Mo and Se atoms had a difference of 46.9 cm^{-1}, as shown in Figure 1b, which is consistent with Raman characteristics of monolayer $MoSe_2$.[56] As for monolayer WS_2, one zone boundary edge phonon LA(M) at 176 cm^{-1} and its intense overtone at 352 cm^{-1} appeared near the Raman mode E_{2g}^1 (356 cm^{-1}), whereas the frequency difference between E_{2g}^1 and A_{1g} (419 cm^{-1}) was 63 cm^{-1}.[57] As for WSe_2, in-plane mode E_{2g}^1 and out-of-plane mode A_{1g} were at 251 and 260 cm^{-1}, respectively; however, the main reason for concluding that WSe_2 is a monolayer material is the absence of Raman peaks at B_{2g}^1 (308 cm^{-1}), owing to the interaction between adjacent layers induced by van der Waals forces instead of the difference between the values of E_{2g}^1 and A_{1g}.[58−60] Besides, the AFM results also prove that the four selected 2D materials are monolayer materials with a thickness less than 1 nm in Figure S2, which is consistent with the conclusion obtained using Raman spectroscopy.[61,62] The absorption and PL spectra of the four monolayer materials are shown in Figure 2. For monolayer 2D materials with a direct bandgap, the minimum value of the conduction band and the maximum value of the valence band are located at the binary indexed corners K^+ and K^- of the 2D hexagonal Brillouin zone, and there are obvious PL peaks for the four materials.[1,12] The enhanced space confinement effect of the exciton wave function and the weakened dielectric screening effect make the binding energy of the exciton approximately 400 meV, and the lack of inversion symmetry and spin−orbit coupling effect result in valley-contrasting strong spin splitting of the valence and conduction bands.[12,45] These effects lead to strong spectrally distinguishable exciton absorption characteristics in the absorption spectra and make the emission peaks of A and B exciton peaks distinguished in the PL spectra of MoS_2 and $MoSe_2$. Among the four materials studied, MoS_2 has the largest full width at half-maximum (fwhm) of the PL spectrum and has a wide spectral range of low-energy edge PL tails, implying a relatively high concentration of defects in MoS_2 among the four materials studied.[53] The detailed exciton spectral characteristics of the four monolayer materials are listed in Table 1.

To study the relaxation kinetics of photogenerated excitons in the four monolayer 2D TMD materials, the transient absorption (TA) spectra were obtained using a femtosecond laser with a wavelength of 520 nm as the pump light, as shown in Figure 3. The negative bleaching peaks were caused by the

Table 1. Experimental Results of A and B Excitons in Absorption and PL Spectra from Figure 2

	absorption spectrum		PL spectrum		
	A exciton (nm)	B exciton (nm)	A exciton (nm)	B exciton (nm)	fwhm (meV)
MoS_2	653.6	606.8	677.2	610.2	130
$MoSe_2$	782.7	692.5	782.9	704.1	57
WS_2	611.9	513.8	623.4		76
WSe_2	734.8	590.2	743.2		56

https://doi.org/10.1021/acsphotonics.1c00932
ACS Photonics XXXX, XXX, XXX−XXX

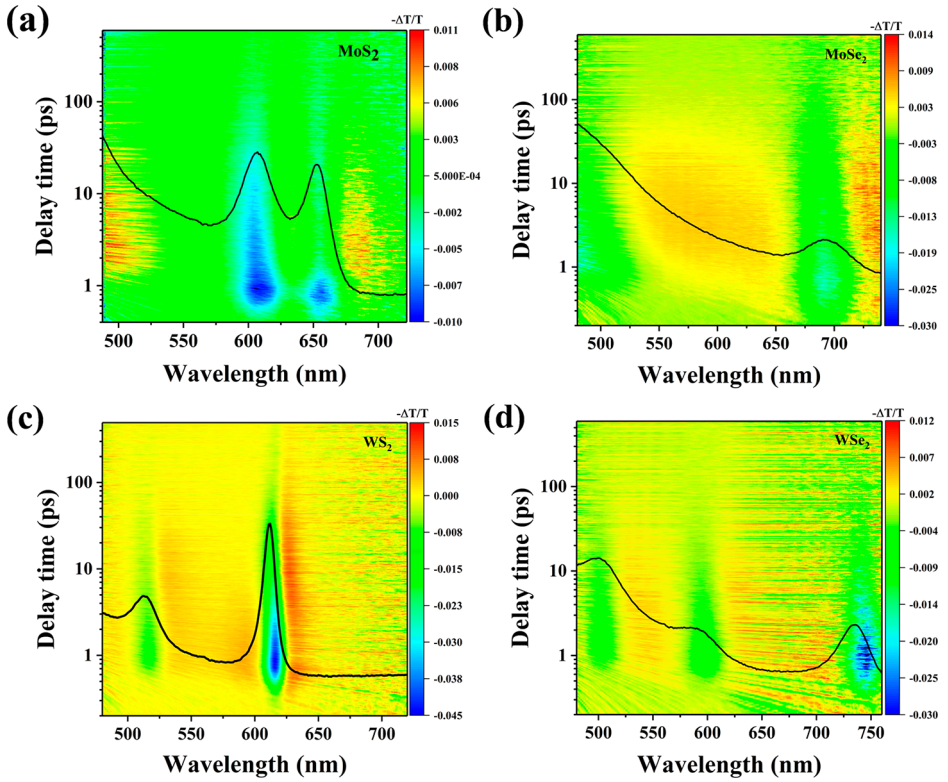

Figure 3. 2D pseudocolor TA spectra of the four CVD-grown monolayer TMDs obtained by pumping at a wavelength of 520 nm for (a) MoS_2, (b) $MoSe_2$, (c) WS_2, and (d) WSe_2 with exciton densities corresponding to 6.8 × 10^{12}/cm^2, 4.2 × 10^{12}/cm^2, 6.08 × 10^{12}/cm^2, and 8.1 × 10^{12}/cm^2, respectively. The black solid line indicates the linear absorption spectrum.

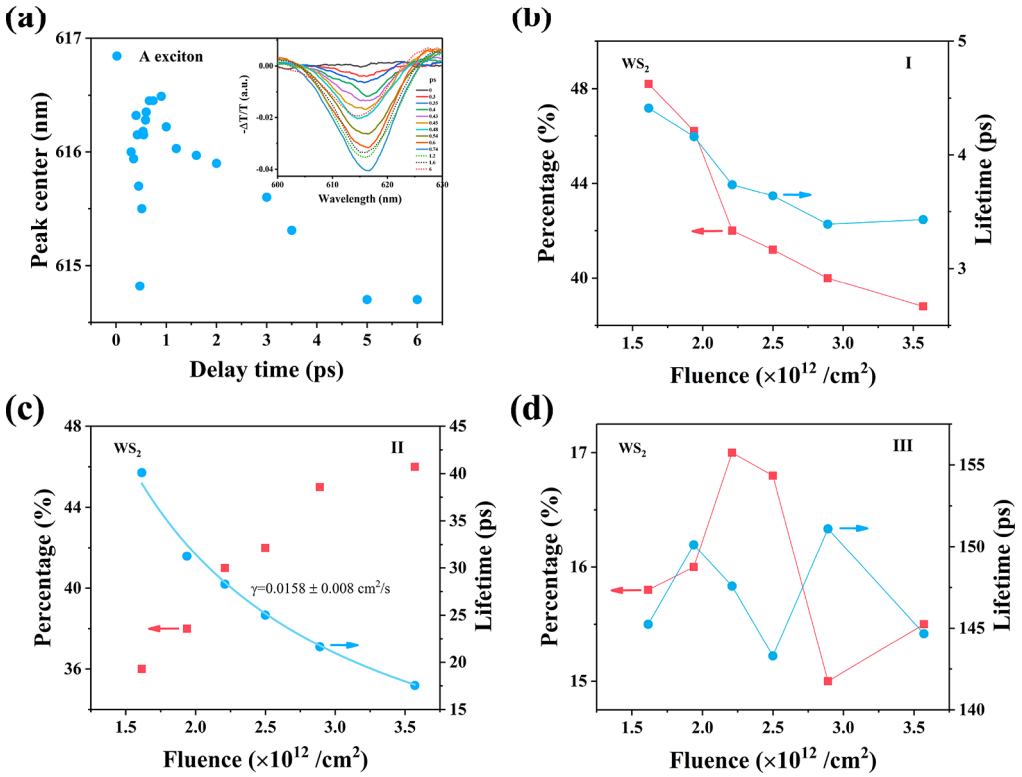

Figure 4. (a) Evolution of the bleaching peak center of the A exciton with delay time in the TAS of WS_2 obtained with exciton density of 6.08 × 10^{12}/cm^2. The inset shows the bleaching peak of the A exciton of WS_2 at different delay times. The exciton densities-dependent percentage (represented by the red quadrilateral) and lifetime (represented by the blue dot) of the three processes corresponding to (b) I, (c) II, and (d) III of the WS_2, respectively. The light blue solid line fitting in process II represents the fitting of the two-body lifetime of the EEA model.

https://doi.org/10.1021/acsphotonics.1c00932
ACS Photonics XXXX, XXX, XXX−XXX

band-filling effect at the exciton absorption peak in the linear absorption spectrum.[18,39] The evolution-associated spectra (EAS) with three different lifetimes were obtained using the global fitting analysis as shown in Figure S3. The TA spectrum of WS_2 was taken as the representative to further analyze the exciton relaxation kinetics as shown in Figure 4a. The A exciton bleaching peak shows a redshift−blueshift physical transition process within approximately 4 ps. This is primarily because of the competition between the transient narrowing of the electron bandgap caused by the exchange-correlation and reduction of the exciton binding energy to increase the optical bandgap caused by increasing the dielectric screening effect of a large of photogenerated carriers in the material.[25,26] With the completion of the thermalization process of hot carriers, the band-filling effect further increases the blueshift of the bleaching peak of A exciton,[39] and the photogenerated carriers undergo the process of interband relaxation. In addition to defect-assisted exciton nonradiation recombination and exciton radiation recombination, the EEA physical process under high excitation intensity is an extremely important physical process that can reduce the PLQY of monolayer materials. Although the defect state can capture the exciton and weaken the EEA process in low and medium exciton densities of approximately 10^{10} cm^{-2},[22,39,46] the effect of defect states on the EEA process has not been examined at high exciton densities below a Mott density of $\sim 10^{13}$ cm^{-2}. Therefore, we further carried out pump fluence-dependent TA spectra experiments to explore the defect state effect on the EEA process at high exciton densities and the differences in EEA physical processes in different monolayer TMD materials.

An accurate relationship between the differential transmission and exciton densities should be established using the pump fluence-dependent TA spectrum. The excitons excited by the pump pulse instantly modulate the absorption of the probe pulse to change the transmission intensity. The density of photogenerated excitons is calculated from the following formula:[19]

$$n_0 = \frac{F\alpha}{\hbar\nu}\varphi \tag{1}$$

where F is the fluence of the pump, α is the absorption coefficient of the monolayer TMDs material obtained from the absorption spectrum in monolayer TMDs materials, mainly because the weak reflected signal can be ignored in the monolayer thin-film material. Here, α takes the value 0.02 for monolayer MoS_2, 0.05 for monolayer $MoSe_2$, 0.024 for monolayer WS_2, and 0.038 for monolayer WSe_2.[46,63] $\hbar\nu$ is the photon energy of the pump, and φ is the ratio of exciton produced perphoton absorbed, which is generally assumed to be unity. In addition, because the lifetime of an exciton is considerably longer than the femtosecond pulse width of the pump light, the attenuation process effect of the exciton during the pump excitation can be ignored to make the exciton density at the bleaching peak near the zero delay time equal to the injected density. Therefore, we associate the differential transmission signal with the differential exciton density, as shown in Figure S4. The peak amplitudes of the A exciton bleaching peak of the four materials become saturated as the exciton density increases; thus, the saturated absorber model (2) can be used to fit the dependence of exciton density as follows:[64]

$$\frac{\Delta T}{T} \propto \frac{n}{n + n_s} \tag{2}$$

where n is the exciton density and n_s is the saturation density. Therefore, the saturation densities were obtained as $4.1 \pm 0.1 \times 10^{12}$, $6.9 \pm 0.5 \times 10^{12}$, $3.29 \pm 0.09 \times 10^{12}$, and $3.83 \pm 0.67 \times 10^{12}$ cm^{-2} for the monolayer MoS_2, $MoSe_2$, WS_2, and WSe_2, respectively, which correspond to the distances between excitons that were 5.5, 4.2, 6.2, and 5.8 nm, respectively. Theoretical calculations and experimental results showed that the exciton Bohr radius of monolayer TMDs is approximately 1−2 nm, and the magnitude corresponding to the exciton density is 10^{13} cm^{-2},[29,39,46,65] which is consistent with the saturation intensity obtained through the Z-scan and two-photon absorption experimental;[4,28,66] hence, the obtained exciton saturation density is acceptable.

When the exciton density is greater than 10^{10} cm^{-2} in monolayer TMDs, the physical process of EEA will dominate the initial relaxation process of excitons, causing a fast relaxation process,[14,39] and the monomolecular recombination, including the single exciton radiation recombination and defect-assisted nonradiation recombination processes, dominate the decay of excitons on longer time scales with lower exciton densities in the material.[38,39,46,47,49] In order to have a more detailed elucidation of the characterization and calculation details of pump fluence-dependent exciton relaxation dynamics, the treatment of the relaxation process of monolayer WS_2 is used as a representation. The intensity of the bleaching signal of the A exciton peak of WS_2 gradually increases with increasing the exciton densities, which was fitted by using the triple exponential decay (Figure S5 and Table S1). The kinetics of A exciton relaxation kinetics of WS_2 can be expressed as the eq 3:[67]

$$g(t) = \sum_{i=1}^{n=3} A_i \ \mathrm{erfc}\left(\frac{\sigma}{\sqrt{2}\,\tau_i} - \frac{t}{\sqrt{2}\,\sigma}\right)\exp\left(-\frac{t}{\tau_i}\right) \tag{3}$$

where A_i and τ_i are the magnitude and lifetime of each component respectively, "erfc" represents the integral error function, and σ is the laser pulse duration. The percentage P of each main component can be calculated by eq 4:

$$P_i = \frac{\sum_{j=t} A_i \ \exp\left(-\frac{t_j}{\tau_i}\right)}{\sum_{j=t}\sum_{i=1}^{n=3} A_i \ \exp\left(-\frac{t_j}{\tau_i}\right)} \tag{4}$$

As shown in Figure 4b, the first fast process "I", with a lifetime of about 3 ps, is characterized by the decreasing proportion and lifetime with increasing the fluence, which is attributed to the processes of excitons trapped by the defect states accompanied by exciton formation and cooling processes at high exciton densities.[14,18] This is because as the pump fluence increases, a large number of defect states are filled or even saturated, resulting in the reduction or even disappearance of the percentage and lifetime of the defect trapping exciton physical process at high exciton densities. For the second process "II" (Figure 4c) with a lifetime of a few tens of ps of the exciton relaxation, the lifetime decreases significantly with increasing excitation intensity, but its proportion increases remarkably. This feature is consistent with the physical process of EEA processes with multibody interactions. We used the two-body lifetime defined as $\tau = -N(0)(dN/dt)^{-1}$ to fit the fluence-dependent lifetime and obtained a good result.[38]

https://doi.org/10.1021/acsphotonics.1c00932
ACS Photonics XXXX, XXX, XXX−XXX

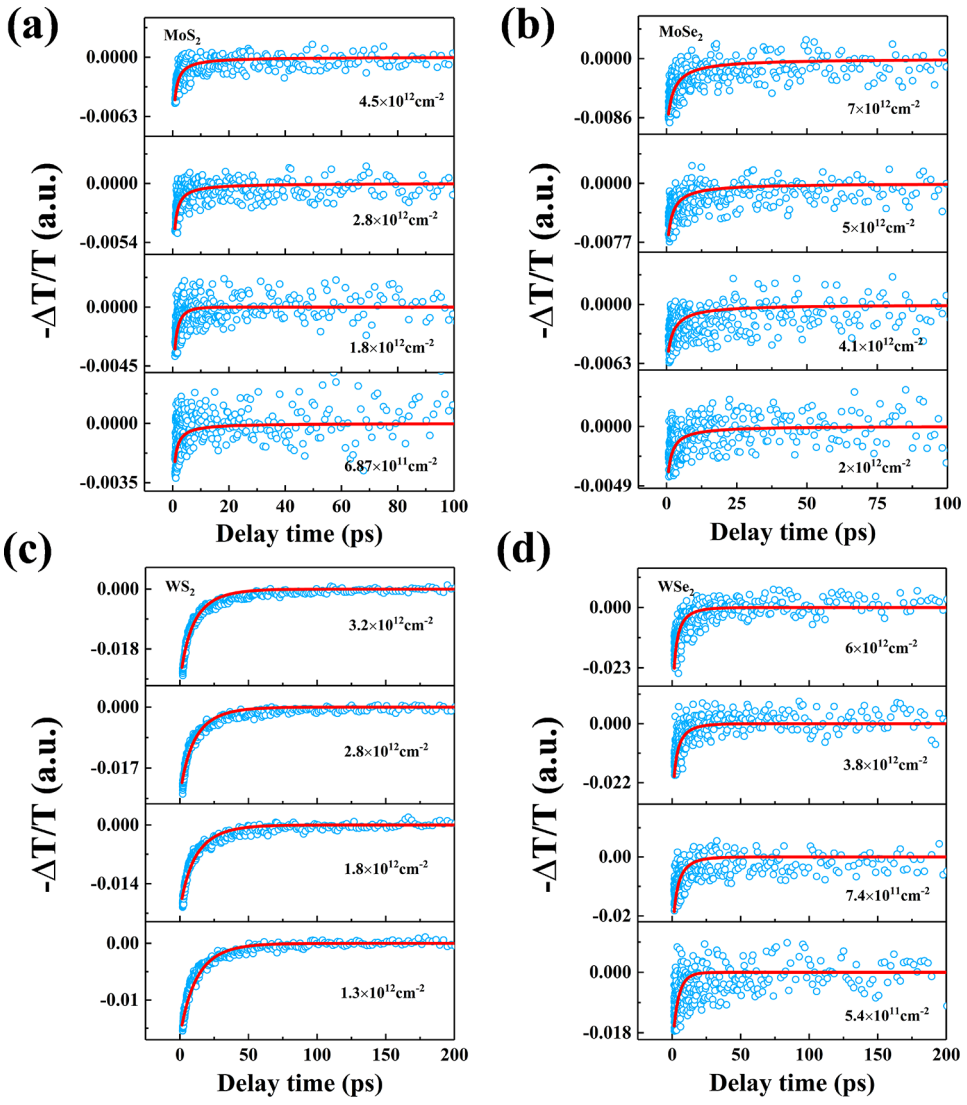

Figure 5. Fluence-dependent relaxation dynamics of A exciton in the four CVD-grown monolayer TMDs: (a) MoS_2, (b) $MoSe_2$, (c) WS_2, and (d) WSe_2.

Table 2. Fit Parameters from Eq 5 for the Four CVD-Grown Monolayer TMDs: (a) MoS_2, (b) $MoSe_2$, (c) WS_2, and (d) WSe_2

	MoS_2	$MoSe_2$	WS_2	WSe_2
τ (ps)	69.4 ± 2	92.2 ± 2	124.665 ± 1	115.8 ± 1
γ (cm^2/s)	0.102 ± 0.01	0.049 ± 0.005	0.016 ± 0.002	0.026 ± 0.003
γ_T (cm^2/s)	0.091	0.046	0.0158	0.0248
$(\gamma n_s)^{-1}$ (ps)	2.48	2.95	18.99	10.04

Therefore, the second process is assigned to the EEA process with the rate of EEA based on the only two-body interactions obtained as 0.0158 ± 0.008 cm^2/s. The third process "III" (Figure 4d) has a 100 ps lifetime with no apparent intensity dependence of lifetime and occupancy, which we attribute to the monomolecular recombination, that is, exciton radiative recombination and defect state-assisted nonradiative recombination process.[38] This is mainly because the single-body recombination process is influenced by its intrinsic properties, which are less affected by the intensity of excitation and are mainly influenced by temperature and material structure factors.[22] In order to further investigate rigorously and systematically the EEA processes of four monolayers at high exciton densities of approximately 10^{12} cm^{-2} below a Mott density of approximately 10^{13} cm^{-2}, we should use a more rigorous recombination model (eq 5) to globally fit the entire set of exciton relaxation dynamics with different exciton densities. The rate equation of exciton population $n(t)$ in this theory can be expressed as follows:

$$\frac{dn(t)}{dt} = -\frac{n(t)}{\tau} - \gamma n(t)^2 \tag{5}$$

$$\frac{1}{\tau} = \frac{1}{\tau_{nr}} + \frac{1}{\tau_r} \tag{6}$$

where τ is the exciton lifetime obtained using eq 5 in the absence of the EEA process, τ_{nr} is the nonradiative lifetime, τ_r is the radiative lifetime, and γ is the assumed time-independent

https://doi.org/10.1021/acsphotonics.1c00932
ACS Photonics XXXX, XXX, XXX−XXX

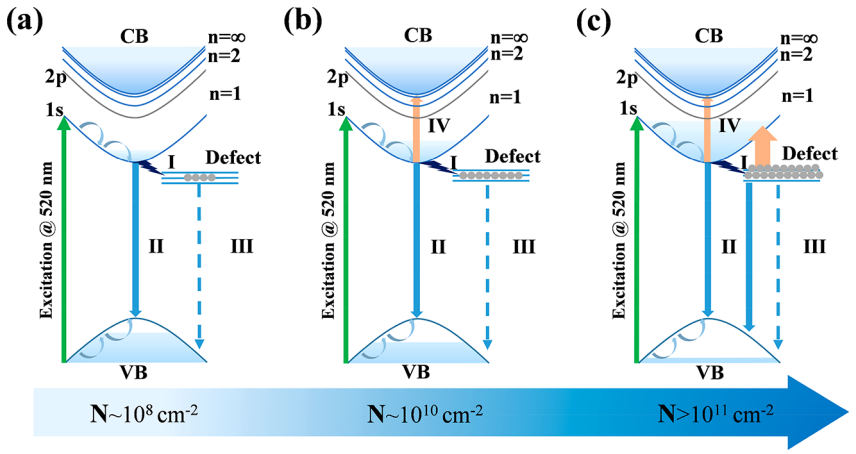

Figure 6. Schematic of the relaxation process of excitons at different exciton concentrations n: (a) low exciton density of $\sim 10^8$ cm^{-2}, (b) medium exciton density of $\sim 10^{10}$ cm^{-2}, and (c) high exciton density of $\sim 10^{12}$ cm^{-2}. VB, CB, and n represent the valence band state, conduction band state, and exciton state, respectively. I (black arrow) indicates the defect capture exciton process, II (light blue arrow) represents the exciton radiation recombination process, III (light blue dotted line arrow) represents the defect-assisted nonradiative recombination process, and IV (beige arrow) indicates the EEA process. Under weak excitation intensity (a), the main relaxation process of excitons is the monomolecular recombination process, that is, exciton radiation recombination and defect state-assisted exciton nonradiative recombination. As the excitation intensity increases to medium exciton density (b), the EEA caused by the two-body interaction of free excitons gradually dominates the exciton recombination process. when the exciton density increases further to high excitation intensity (c), the EEA process is enhanced by the many-body interaction of local excitons captured by defects and greatly reduces the proportion of exciton radiative recombination.

annihilation rate. Studies of ultrafast carrier dynamics suggest that the lifetime of the carrier valley relaxation process is about a few picoseconds.[68,69] So, in order to exclude the effect of valley relaxation on the EEA process due to differences in materials, we fit the EEA process starting at 4 ps. Equation 5 provides a reasonable global fit to the entire set of A exciton relaxation dynamics for different initial exciton densities with a single set of parameters, as shown in Figure 5, suggesting that the EEA process becomes the dominant recombination mechanism in the monolayer TMDs at an exciton concentration of approximately 10^{11} cm^{-2}. The exciton lifetime and annihilation rates are listed in Table 2, in which the magnitude of EEA rate is close to the reported results for monolayer TMDs.[37−39,46] For the monolayer WS_2, the rate γ of EEA obtained by the fitting of eq 5 coincides with γ_T obtained by the second process "II" mentioned in the previous content, indicating the reasonableness and validity of our fitted parameters. Figure 2 shows that the steady-state PL intensity of WS_2 is the highest, followed by those of WSe_2, $MoSe_2$, and MoS_2 under the same experimental conditions, which means the PLQY of WS_2 is the highest, followed by those of WSe_2, $MoSe_2$, and MoS_2. Besides, the monomolecular lifetime τ of WS_2 was the longest, followed by those of WSe_2, $MoSe_2$, and MoS_2, which was determined by the EEA model. Combining the results of steady-state PL with the monomolecular lifetime τ, the conclusion can be obtained that WS_2 has the lowest defect density of states, followed by WSe_2, $MoSe_2$, and MoS_2.[70] Jung et al. confirmed that chalcogen-atom vacancies inducing two midgap states around valence band edges (singlet a1 states) and inside energy gaps (doublet e states) are the most prevalent atomic defects in monolayer TMDs (WS_2, MoS_2, WSe_2, and $MoSe_2$).[53] They revealed that WS_2 inherently has isolated sulfur-atom vacancies, the intrinsic MoS_2, $MoSe_2$, and WSe_2 films are inclined to possess hybridized vacancy chains based on chalcogen-atom vacancies. So the monolayer WS_2 has the lowest density of defective states, which agrees with the above-mentioned conclusions. Since the defect states can capture and localize excitons whose density in monolayer 2D TMDs up to almost 10^{12} cm^{-2},[53,71] they also can increase the exciton saturation density in monolayer TMDs.[47] Therefore, WS_2 exhibits the smallest exciton saturation density, which is consistent with the results obtained using the saturated absorber model, as shown in Figure S4.

The validity of two-body interactions, such as EEA produced by high excitation fluence, can be verified by comparing the monomolecular lifetime τ and the effective lifetime $(\gamma n)^{-1}$, which depends on the exciton density. For the four kinds of monolayer TMDs, when the excitation intensity is close to the exciton saturation density n_s, the effective lifetime $(\gamma n_s)^{-1}$ is considerably less than the monomolecular lifetime τ by nearly one order of magnitude, as shown in Table 2. Thus, the rapid relaxation process primarily originates from the nonlinear many-body interaction, and the monomolecular recombination process can be ignored when the exciton density is close to the exciton saturation density. We further find that with the increase of the density of defect states in the material, the effective lifetime $(\gamma n_s)^{-1}$ of the EEA process decreases, especially in the MoS_2 samples with the highest defect concentration. The results indicate that EEA can be enhanced by the defect state when the exciton density is greater than 10^{11} cm^{-2} in monolayer TMDs. It can be seen from $\gamma = 4\pi D r_a$ that the EEA is essentially affected by the diffusion constant D and the distance r_a between the excitons when exciton collision occurs.[72] Since the exciton binding energy affects the exciton radius, as the exciton binding energy of WS_2, WSe_2, MoS_2, and $MoSe_2$ increases, where the exciton binding energies of monolayer WS_2, WSe_2, MoS_2, and $MoSe_2$ are 320, 370, 500, and 550 meV, respectively, the exciton radii of WS_2, WSe_2, MoS_2, and $MoSe_2$ become smaller.[13,16,73,74] So the probability of collision between excitons becomes increasingly smaller under the condition of the same exciton density to make the EEA rate smaller. However, this conclusion is inconsistent with the results obtained using the EEA model fitting. This is predominantly because the effect of defect states on the exciton diffusion is ignored, and the material we studied is a polycrystalline monolayer continuous film whose defect state

https://doi.org/10.1021/acsphotonics.1c00932
ACS Photonics XXXX, XXX, XXX−XXX

density is considerably higher than that of monolayer single-crystal material.[38,47] Although the defect state-assisted single-exciton relaxation channel weakens the EEA effect at lower exciton densities,[20,39,47,50] defect states can further improve the probability of exciton collision as the local exciton density in defect states increases. Therefore, the EEA process of local excitons is enhanced by the defect state and plays a key role in the exciton relaxation process when the exciton density is close to the exciton saturation density. A schematic of the relaxation process of excitons at different exciton concentrations is shown in Figure 6. Under weak excitation intensities, the main relaxation process of excitons is the monomolecular recombination process, that is, exciton radiation recombination and defect state-assisted exciton nonradiative recombination. As the excitation intensity increases to medium exciton density, the EEA caused by the two-body interaction of free excitons gradually dominates the exciton recombination process. when the exciton density increases further to high excitation intensity, the EEA process is enhanced by the many-body interaction of local excitons captured by defects and greatly reduces the proportion of exciton radiative recombination. The density of defect states in monolayer MoS_2 is the highest compared to those of the other test samples obtained from the above, which results in the maximum rate of EEA.[75] For monolayer $MoSe_2$, WSe_2, and WS_2, as the defect density decreases, the EEA rate gets smaller. In order to decrease the enhancement of the EEA by defects at high excitation intensities, the defect engineering is needed to reduce the density of defect states in materials and further improves the performance of TMDs-based light-emitting devices.[17,70,76]

In summary, we employed femtosecond TA spectroscopy to investigate the exciton dynamics of monolayer continuous-film TMDs (i.e., MoS_2, WSe_2, WS_2, and WSe_2) grown via CVD. We demonstrated that the defect-assisted EEA process is enhanced and plays a key role in the carrier relaxation process under an exciton density exceeding approximately 10^{12} cm^{-2}. The measured EEA rates for WS_2, WSe_2, $MoSe_2$, and MoS_2 were 0.016, 0.026, 0.049, and 0.102 cm^2/s, respectively, implying that EEA is enhanced as the defect states increase in monolayer TMDs. The results of this study help in elucidating the effect of defect states on exciton−exciton interactions in monolayer TMDs and optimizing the quantum yield of advanced light-emitting devices and high-efficiency photodetectors based on TMDs.

METHODS

PL Measurements. Monolayer continuous-film TMDs (i.e., MoS_2, WSe_2, WS_2, and WSe_2), prepared on silica substrates, were excited by CW laser excitation at a wavelength of 473 nm and a power density of 2 $\mu J \cdot cm^{-2}$. PL was separated by 150 g/mm grating using a monochromator supplied by Princeton Instruments (model: SP2500). Subsequently, the spectral information was collected using PIXIS-100BX CCD at −75 °C.

Raman Spectra. Raman spectra of polycrystalline thin films, prepared on silica substrates, were obtained with a Raman spectrometer (LHA19120048) using a CW laser (532 nm) as the emission source at room temperature. Raman mapping within a rectangle with a side length of 60 μm, in 1 μm steps, and the spot of the laser is 1 μm.

UV/Visible Absorption. UV−vis absorption spectra of polycrystalline thin films, prepared on glass substrates, were collected using a Lambda 950 UV−vis spectrometer.

Transient Absorption (TA) Measurements. Femtosecond TA spectroscopy measurements of polycrystalline thin films, prepared on quartz substrates, were performed using our custom-built TAS setup. The light pulse generated by the Spectra-Physics Spirit laser (350 fs, 1 kHz, 40 μJ/pulse) is split into two parts by an ultrafast beam splitter with a reflection to transmission energy ratio of 1:4. A frequency-doubled 520 nm output from the transmitted light was used as the pump beam, whereas the reflected laser pulse was used to excite a sapphire crystal for generating white light continuous (WLC) spectrum, whose chirp effect is corrected. The pump beam was chopped at 500 Hz, and the probe beam transmitting the sample is collected by an ultrafast fiber optic spectrometer after passing through a short pass filter with a cutoff wavelength of 950 nm. The time window of the TA measurement was 1.6 ns. The spot radii of pump light and probe light are determined to be 20.5 ± 0.5 and 5 ± 0.5 μm, respectively, by the knife-cut method, and the pump light and probe light overlap at the same point of the sample in a noncollinear manner. All the experiments are carried out at 300 K, and the calculation method of exciton density excited by pump light in the material is given in detail in the manuscript.

ASSOCIATED CONTENT

Supporting Information

The Supporting Information is available free of charge at https://pubs.acs.org/doi/10.1021/acsphotonics.1c00932.

Experimental data of the optical microscope images and Raman mapping (Figure S1) and AFM results (Figure S2), EAS and DAS spectra (Figure S3), calculation of saturation intensity (Figure S4), and fitting results (Figure S5 and Table S1) (PDF)

AUTHOR INFORMATION

Corresponding Author

Jun Wang − *Laboratory of Micro-Nano Optoelectronic Materials and Devices, Key Laboratory of Materials for High-Power Laser, State Key Laboratory of High Field Laser Physics, Shanghai Institute of Optics and Fine Mechanics, Chinese Academy of Sciences, Shanghai 201800, China; Center of Materials Science and Optoelectronic Engineering, University of Chinese Academy of Sciences, Beijing 100049, China; CAS Center for Excellence in Ultra-intense Laser Science, Shanghai 201800, China;* orcid.org/0000-0003-0064-3551; Email: jwang@siom.ac.cn

Author

Tianju Zhang − *Laboratory of Micro-Nano Optoelectronic Materials and Devices, Key Laboratory of Materials for High-Power Laser, State Key Laboratory of High Field Laser Physics, Shanghai Institute of Optics and Fine Mechanics, Chinese Academy of Sciences, Shanghai 201800, China; Center of Materials Science and Optoelectronic Engineering, University of Chinese Academy of Sciences, Beijing 100049, China*

Complete contact information is available at: https://pubs.acs.org/10.1021/acsphotonics.1c00932

Notes

The authors declare no competing financial interest.

■ ACKNOWLEDGMENTS

This work is supported by NSFC (no. 61975221) and the Strategic Priority Research Program of CAS (nos. XDB16030700 and XDB43010303).

■ REFERENCES

(1) Splendiani, A.; Sun, L.; Zhang, Y.; Li, T.; Kim, J.; Chim, C. Y.; Galli, G.; Wang, F. Emerging photoluminescence in monolayer MoS_2. *Nano Lett.* **2010**, *10* (4), 1271−1275.
(2) Miao, X.; Zhang, G.; Wang, F.; Yan, H.; Ji, M. Layer-Dependent Ultrafast Carrier and Coherent Phonon Dynamics in Black Phosphorus. *Nano Lett.* **2018**, *18* (5), 3053−3059.
(3) Liu, Y.; Hu, X.; Wang, T.; Liu, D. Reduced Binding Energy and Layer-Dependent Exciton Dynamics in Monolayer and Multilayer WS_2. *ACS Nano* **2019**, *13* (12), 14416−14425.
(4) Xie, Y.; Zhang, S.; Li, Y.; Dong, N.; Zhang, X.; Wang, L.; Liu, W.; Kislyakov, I. M.; Nunzi, J.-M.; Qi, H.; Zhang, L.; Wang, J. Layer-modulated two-photon absorption in MoS_2: probing the shift of the excitonic dark state and band-edge. *Photon. Res.* **2019**, *7* (7), 762−770.
(5) Zhang, G.; Huang, S.; Wang, F.; Yan, H. Layer-Dependent Electronic and Optical Properties of 2D Black Phosphorus: Fundamentals and Engineering. *Laser Photonics Rev.* **2021**, *15*, 2000399.
(6) Li, J.; Mao, X.; Xie, S.; Geng, Z.; Chen, H. Bipolar phototransistor in a vertical Au/graphene/MoS_2 van der Waals heterojunction with photocurrent enhancement. *Photon. Res.* **2020**, *8* (1), 39−45.
(7) Dery, H.; Song, Y. Polarization analysis of excitons in monolayer and bilayer transition-metal dichalcogenides. *Phys. Rev. B: Condens. Matter Mater. Phys.* **2015**, *92* (12), 125431.
(8) Guddala, S.; Kawaguchi, Y.; Komissarenko, F.; Kiriushechkina, S.; Vakulenko, A.; Chen, K.; Alu, A.; M. Menon, V.; Khanikaev, A. B. All-optical nonreciprocity due to valley polarization pumping in transition metal dichalcogenides. *Nat. Commun.* **2021**, *12* (1), 3746.
(9) Ko, B. A.; Sokolov, A. V.; Scully, M. O.; Zhang, Z. R.; Lee, H. W. H. Enhanced four-wave mixing process near the excitonic resonances of bulk MoS_2. *Photon. Res.* **2019**, *7* (3), 251−259.
(10) Fu, Q.; Hu, Z. L.; Zhou, M. F.; Lu, J. P.; Ni, Z. H. Excitonic Emission in Atomically Thin Electroluminescent Devices. *Laser Photonics Rev.* **2021**, *15*, 2000587.
(11) Wang, J.; Verzhbitskiy, I.; Eda, G. Electroluminescent Devices Based on 2D Semiconducting Transition Metal Dichalcogenides. *Adv. Mater.* **2018**, *30* (47), 1802687.
(12) Kozawa, D.; Kumar, R.; Carvalho, A.; Kumar Amara, K.; Zhao, W.; Wang, S.; Toh, M.; Ribeiro, R. M.; Castro Neto, A. H.; Matsuda, K.; Eda, G. Photocarrier relaxation pathway in two-dimensional semiconducting transition metal dichalcogenides. *Nat. Commun.* **2014**, *5*, 4543.
(13) He, K.; Kumar, N.; Zhao, L.; Wang, Z.; Mak, K. F.; Zhao, H.; Shan, J. Tightly bound excitons in monolayer WSe_2. *Phys. Rev. Lett.* **2014**, *113* (2), 026803.
(14) Cunningham, P. D.; Hanbicki, A. T.; McCreary, K. M.; Jonker, B. T. Photoinduced Bandgap Renormalization and Exciton Binding Energy Reduction in WS_2. *ACS Nano* **2017**, *11* (12), 12601−12608.
(15) Hill, H. M.; Rigosi, A. F.; Roquelet, C.; Chernikov, A.; Berkelbach, T. C.; Reichman, D. R.; Hybertsen, M. S.; Brus, L. E.; Heinz, T. F. Observation of Excitonic Rydberg States in Monolayer MoS_2 and WS_2 by Photoluminescence Excitation Spectroscopy. *Nano Lett.* **2015**, *15* (5), 2992−2997.
(16) Chernikov, A.; Berkelbach, T. C.; Hill, H. M.; Rigosi, A.; Li, Y.; Aslan, O. B.; Reichman, D. R.; Hybertsen, M. S.; Heinz, T. F. Exciton binding energy and nonhydrogenic Rydberg series in monolayer WS_2. *Phys. Rev. Lett.* **2014**, *113* (7), 076802.
(17) Amani, M.; Lien, D. H.; Kiriya, D.; Xiao, J.; Azcatl, A.; Noh, J.; Madhvapathy, S. R.; Addou, R.; Kc, S.; Dubey, M.; Cho, K.; Wallace, R. M.; Lee, S. C.; He, J. H.; Ager, J. W., 3rd; Zhang, X.; Yablonovitch, E.; Javey, A. Near-unity photoluminescence quantum yield in MoS_2. *Science* **2015**, *350* (6264), 1065−8.
(18) Shi, H.; Yan, R.; Bertolazzi, S.; Brivio, J.; Gao, B.; Kis, A.; Jena, D.; Xing, H. G.; Huang, L. Exciton dynamics in suspended monolayer and few-layer MoS_2 2D crystals. *ACS Nano* **2013**, *7* (2), 1072−1080.
(19) Chernikov, A.; Ruppert, C.; Hill, H. M.; Rigosi, A. F.; Heinz, T. F. Population inversion and giant bandgap renormalization in atomically thin WS_2 layers. *Nat. Photonics* **2015**, *9* (7), 466−470.
(20) Wang, H.; Zhang, C.; Rana, F. Ultrafast dynamics of defect-assisted electron-hole recombination in monolayer MoS_2. *Nano Lett.* **2015**, *15* (1), 339−345.
(21) Wang, H.; Zhang, C.; Rana, F. Surface Recombination Limited Lifetimes of Photoexcited Carriers in Few-Layer Transition Metal Dichalcogenide MoS_2. *Nano Lett.* **2015**, *15* (12), 8204−8210.
(22) Yuan, L.; Huang, L. Exciton dynamics and annihilation in WS_2 2D semiconductors. *Nanoscale* **2015**, *7* (16), 7402−7408.
(23) Pogna, E. A.; Marsili, M.; De Fazio, D.; Dal Conte, S.; Manzoni, C.; Sangalli, D.; Yoon, D.; Lombardo, A.; Ferrari, A. C.; Marini, A.; Cerullo, G.; Prezzi, D. Photo-Induced Bandgap Renormalization Governs the Ultrafast Response of Single-Layer MoS_2. *ACS Nano* **2016**, *10* (1), 1182−1188.
(24) Ruppert, C.; Chernikov, A.; Hill, H. M.; Rigosi, A. F.; Heinz, T. F. The Role of Electronic and Phononic Excitation in the Optical Response of Monolayer WS_2 after Ultrafast Excitation. *Nano Lett.* **2017**, *17* (2), 644−651.
(25) Sie, E. J.; Steinhoff, A.; Gies, C.; Lui, C. H.; Ma, Q.; Rosner, M.; Schonhoff, G.; Jahnke, F.; Wehling, T. O.; Lee, Y. H.; Kong, J.; Jarillo-Herrero, P.; Gedik, N. Observation of Exciton Redshift-Blueshift Crossover in Monolayer WS_2. *Nano Lett.* **2017**, *17* (7), 4210−4216.
(26) Liu, F.; Ziffer, M. E.; Hansen, K. R.; Wang, J.; Zhu, X. Direct Determination of Band-Gap Renormalization in the Photoexcited Monolayer MoS_2. *Phys. Rev. Lett.* **2019**, *122* (24), 246803.
(27) Wang, L.; Wang, Z.; Wang, H. Y.; Grinblat, G.; Huang, Y. L.; Wang, D.; Ye, X. H.; Li, X. B.; Bao, Q.; Wee, A. S.; Maier, S. A.; Chen, Q. D.; Zhong, M. L.; Qiu, C. W.; Sun, H. B. Slow cooling and efficient extraction of C-exciton hot carriers in MoS_2 monolayer. *Nat. Commun.* **2017**, *8*, 13906.
(28) Dong, N. N.; Li, Y. X.; Zhang, S. F.; McEvoy, N.; Gatensby, R.; Duesberg, G. S.; Wang, J. Saturation of Two-Photon Absorption in Layered Transition Metal Dichalcogenides: Experiment and Theory. *ACS Photonics* **2018**, *5* (4), 1558−1565.
(29) Mak, K. F.; Shan, J. Photonics and optoelectronics of 2D semiconductor transition metal dichalcogenides. *Nat. Photonics* **2016**, *10* (4), 216−226.
(30) Lopez-Sanchez, O.; Lembke, D.; Kayci, M.; Radenovic, A.; Kis, A. Ultrasensitive photodetectors based on monolayer MoS_2. *Nat. Nanotechnol.* **2013**, *8* (7), 497−501.
(31) Xiao, J.; Zhao, M.; Wang, Y.; Zhang, X. Excitons in atomically thin 2D semiconductors and their applications. *Nanophotonics* **2017**, *6* (6), 1309−1328.
(32) Wu, Y.; Li, Z.; Ang, K.-W.; Jia, Y.; Shi, Z.; Huang, Z.; Yu, W.; Sun, X.; Liu, X.; Li, D. Monolithic integration of MoS2-based visible detectors and GaN-based UV detectors. *Photon. Res.* **2019**, *7* (10), 1127−1133.
(33) Gao, S.; Wang, Z. Q.; Wang, H. D.; Meng, F. X.; Wang, P. F.; Chen, S.; Zeng, Y. H.; Zhao, J. L.; Hu, H. G.; Cao, R.; Xu, Z. Q.; Guo, Z. N.; Zhang, H. Graphene/MoS_2/Graphene Vertical Heterostructure-Based Broadband Photodetector with High Performance. *Adv. Mater. Interfaces* **2021**, *8* (3), 2001730.
(34) Radisavljevic, B.; Radenovic, A.; Brivio, J.; Giacometti, V.; Kis, A. Single-layer MoS_2 transistors. *Nat. Nanotechnol.* **2011**, *6* (3), 147−150.
(35) Chernikov, A.; van der Zande, A. M.; Hill, H. M.; Rigosi, A. F.; Velauthapillai, A.; Hone, J.; Heinz, T. F. Electrical Tuning of Exciton Binding Energies in Monolayer WS_2. *Phys. Rev. Lett.* **2015**, *115* (12), 126802.
(36) Fernandez, H. A.; Withers, F.; Russo, S.; Barnes, W. L. Electrically Tuneable Exciton-Polaritons through Free Electron

https://doi.org/10.1021/acsphotonics.1c00932
ACS Photonics XXXX, XXX, XXX−XXX

Doping in Monolayer WS_2 Microcavities. *Adv. Opt. Mater.* **2019**, *7* (18), 1900484.
(37) Mouri, S.; Miyauchi, Y.; Toh, M.; Zhao, W.; Eda, G.; Matsuda, K. Nonlinear photoluminescence in atomically thin layered WSe_2 arising from diffusion-assisted exciton-exciton annihilation. *Phys. Rev. B: Condens. Matter Mater. Phys.* **2014**, *90* (15), 155449.
(38) Sun, D.; Rao, Y.; Reider, G. A.; Chen, G.; You, Y.; Brezin, L.; Harutyunyan, A. R.; Heinz, T. F. Observation of rapid exciton-exciton annihilation in monolayer molybdenum disulfide. *Nano Lett.* **2014**, *14* (10), 5625−5629.
(39) Cunningham, P. D.; McCreary, K. M.; Jonker, B. T. Auger Recombination in Chemical Vapor Deposition-Grown Monolayer WS_2. *J. Phys. Chem. Lett.* **2016**, *7* (24), 5242−5246.
(40) Ma, Y. Z.; Valkunas, L.; Dexheimer, S. L.; Bachilo, S. M.; Fleming, G. R. Femtosecond spectroscopy of optical excitations in single-walled carbon nanotubes: evidence for exciton-exciton annihilation. *Phys. Rev. Lett.* **2005**, *94* (15), 157402.
(41) Huang, L.; Krauss, T. D. Quantized bimolecular auger recombination of excitons in single-walled carbon nanotubes. *Phys. Rev. Lett.* **2006**, *96* (5), 057407.
(42) Li, Q.; Yang, Y.; Que, W.; Lian, T. Size-and Morphology-Dependent Auger Recombination in $CsPbBr_3$ Perovskite Two-Dimensional Nanoplatelets and One-Dimensional Nanorods. *Nano Lett.* **2019**, *19* (8), 5620−5627.
(43) Klimov, V. V.; Mikhailovsky, A. A.; McBranch, D. W.; Leatherdale, C. A.; Bawendi, M. G. Quantization of multiparticle auger rates in semiconductor quantum dots. *Science* **2000**, *287* (5455), 1011−1013.
(44) Fennel, F.; Lochbrunner, S. Exciton−exciton annihilation in a disordered molecular system by direct and multistep Förster transfer. *Phys. Rev. B: Condens. Matter Mater. Phys.* **2015**, *92* (14), 140301.
(45) Lee, K. J.; Xin, W.; Guo, C. Annihilation mechanism of excitons in a MoS_2 monolayer through direct Förster-type energy transfer and multistep diffusion. *Phys. Rev. B: Condens. Matter Mater. Phys.* **2020**, *101* (19), 195407.
(46) Kumar, N.; Cui, Q.; Ceballos, F.; He, D.; Wang, Y.; Zhao, H. Exciton-exciton annihilation in $MoSe_2$ monolayers. *Phys. Rev. B: Condens. Matter Mater. Phys.* **2014**, *89* (12), 125427.
(47) Surrente, A.; Mitioglu, A. A.; Galkowski, K.; Klopotowski, L.; Tabis, W.; Vignolle, B.; Maude, D. K.; Plochocka, P. Onset of exciton-exciton annihilation in single-layer black phosphorus. *Phys. Rev. B: Condens. Matter Mater. Phys.* **2016**, *94* (7), 075425.
(48) Surrente, A.; Mitioglu, A. A.; Galkowski, K.; Tabis, W.; Maude, D. K.; Plochocka, P. Excitons in atomically thin black phosphorus. *Phys. Rev. B: Condens. Matter Mater. Phys.* **2016**, *93* (12), 121405.
(49) Yu, Y. L.; Yu, Y. F.; Xu, C.; Barrette, A.; Gundogdu, K.; Cao, L. Y. Fundamental limits of exciton-exciton annihilation for light emission in transition metal dichalcogenide monolayers. *Phys. Rev. B: Condens. Matter Mater. Phys.* **2016**, *93* (20), 201111.
(50) Wang, H. N.; Strait, J. H.; Zhang, C. J.; Chan, W. M.; Manolatou, C.; Tiwari, S.; Rana, F. Fast exciton annihilation by capture of electrons or holes by defects via Auger scattering in monolayer metal dichalcogenides. *Phys. Rev. B: Condens. Matter Mater. Phys.* **2015**, *91* (16), 165411.
(51) Jiang, X.; Zheng, Q.; Lan, Z.; Saidi, W. A.; Ren, X.; Zhao, J. Real-time GW-BSE investigations on spin-valley exciton dynamics in monolayer transition metal dichalcogenide. *Sci. Adv.* **2021**, *7* (10), eabf3759.
(52) Cappelluti, E.; Roldán, R.; Silva-Guillén, J. A.; Ordejón, P.; Guinea, F. Tight-binding model and direct-gap/indirect-gap transition in single-layer and multilayer MoS2. *Phys. Rev. B: Condens. Matter Mater. Phys.* **2013**, *88* (7), 075409.
(53) Jeong, T. Y.; Kim, H.; Choi, S. J.; Watanabe, K.; Taniguchi, T.; Yee, K. J.; Kim, Y. S.; Jung, S. Spectroscopic studies of atomic defects and bandgap renormalization in semiconducting monolayer transition metal dichalcogenides. *Nat. Commun.* **2019**, *10* (1), 3825.
(54) Quellmalz, A.; Wang, X.; Sawallich, S.; Uzlu, B.; Otto, M.; Wagner, S.; Wang, Z.; Prechtl, M.; Hartwig, O.; Luo, S.; Duesberg, G. S.; Lemme, M. C.; Gylfason, K. B.; Roxhed, N.; Stemme, G.; Niklaus, F. Large-area integration of two-dimensional materials and their heterostructures by wafer bonding. *Nat. Commun.* **2021**, *12* (1), 917.
(55) Li, H.; Zhang, Q.; Yap, C. C. R.; Tay, B. K.; Edwin, T. H. T.; Olivier, A.; Baillargeat, D. From Bulk to Monolayer MoS_2: Evolution of Raman Scattering. *Adv. Funct. Mater.* **2012**, *22* (7), 1385−1390.
(56) Xia, J.; Huang, X.; Liu, L.-Z.; Wang, M.; Wang, L.; Huang, B.; Zhu, D.-D.; Li, J.-J.; Gu, C.-Z.; Meng, X.-M. CVD synthesis of large-area, highly crystalline $MoSe_2$ atomic layers on diverse substrates and application to photodetectors. *Nanoscale* **2014**, *6* (15), 8949−8955.
(57) Gaur, A. P. S.; Sahoo, S.; Scott, J. F.; Katiyar, R. S. Electron−Phonon Interaction and Double-Resonance Raman Studies in Monolayer WS_2. *J. Phys. Chem. C* **2015**, *119* (9), 5146−5151.
(58) Liu, B.; Fathi, M.; Chen, L.; Abbas, A.; Ma, Y.; Zhou, C. Chemical Vapor Deposition Growth of Monolayer WSe_2 with Tunable Device Characteristics and Growth Mechanism Study. *ACS Nano* **2015**, *9* (6), 6119−6127.
(59) Sahin, H.; Tongay, S.; Horzum, S.; Fan, W.; Zhou, J.; Li, J.; Wu, J.; Peeters, F. M. Anomalous Raman spectra and thickness-dependent electronic properties of WSe_2. *Phys. Rev. B: Condens. Matter Mater. Phys.* **2013**, *87* (16), 165409.
(60) Huang, J.; Yang, L.; Liu, D.; Chen, J.; Fu, Q.; Xiong, Y.; Lin, F.; Xiang, B. Large-area synthesis of monolayer WSe_2 on a SiO_2/Si substrate and its device applications. *Nanoscale* **2015**, *7* (9), 4193−4198.
(61) Shim, J.; Bae, S. H.; Kong, W.; Lee, D.; Qiao, K.; Nezich, D.; Park, Y. J.; Zhao, R. K.; Sundaram, S.; Li, X.; Yeon, H.; Choi, C.; Kum, H.; Yue, R. Y.; Zhou, G. Y.; Ou, Y. B.; Lee, K.; Moodera, J.; Zhao, X. H.; Ahn, J. H.; Hinkle, C.; Ougazzaden, A.; Kim, J. Controlled crack propagation for atomic precision handling of wafer-scale two-dimensional materials. *Science* **2018**, *362* (6415), 665−670.
(62) Poudel, Y.; Sławińska, J.; Gopal, P.; Seetharaman, S.; Hennighausen, Z.; Kar, S.; D'souza, F.; Nardelli, M. B.; Neogi, A. Absorption and emission modulation in a MoS_2−GaN (0001) heterostructure by interface phonon−exciton coupling. *Photon. Res.* **2019**, *7* (12), 1511−1520.
(63) Beal, A. R.; Hughes, H. P. Kramers-Kronig Analysis of the Reflectivity Spectra of 2H-MoS_2, 2H-$MoSe_2$ and 2H-$MoTe_2$. *J. Phys. C: Solid State Phys.* **1979**, *12* (5), 881−890.
(64) Yu, Y.; Zhang, X. K.; Zhou, Z. K.; Zhang, Z.; Bao, Y. J.; Xu, H. F.; Lin, L. M.; Zhang, Y.; Wang, X. H. Microscopic pump-probe optical technique to characterize the defect of monolayer transition metal dichalcogenides. *Photon. Res.* **2019**, *7* (7), 711−721.
(65) Li, J.; Zhong, Y. L.; Zhang, D. Excitons in monolayer transition metal dichalcogenides. *J. Phys.: Condens. Matter* **2015**, *27* (31), 315301.
(66) Li, Y.; Dong, N.; Zhang, S.; Zhang, X.; Feng, Y.; Wang, K.; Zhang, L.; Wang, J. Giant two-photon absorption in monolayer MoS_2. *Laser Photonics Rev.* **2015**, *9* (4), 427−434.
(67) Chen, S. L.; Zhang, T. J.; Liu, X. L.; Qiao, J. L.; Peng, L.; Wang, J.; Liu, Y. S.; Yang, T. Y.; Lin, J. Lattice reconstruction of La-incorporated CsPbI2Br with suppressed phase transition for air-processed all-inorganic perovskite solar cells. *J. Mater. Chem. C* **2020**, *8* (10), 3351−3358.
(68) Zhu, C. R.; Zhang, K.; Glazov, M.; Urbaszek, B.; Amand, T.; Ji, Z. W.; Liu, B. L.; Marie, X. Exciton valley dynamics probed by Kerr rotation in WSe_2 monolayers. *Phys. Rev. B: Condens. Matter Mater. Phys.* **2014**, *90* (16), 161302.
(69) Dal Conte, S.; Bottegoni, F.; Pogna, E. A. A.; De Fazio, D.; Ambrogio, S.; Bargigia, I.; D'Andrea, C.; Lombardo, A.; Bruna, M.; Ciccacci, F.; Ferrari, A. C.; Cerullo, G.; Finazzi, M. Ultrafast valley relaxation dynamics in monolayer MoS_2 probed by nonequilibrium optical techniques. *Phys. Rev. B: Condens. Matter Mater. Phys.* **2015**, *92* (23), 235425.
(70) Dai, X.; Zhang, X.; Kislyakov, I. M.; Wang, L.; Huang, J.; Zhang, S.; Dong, N.; Wang, J. Enhanced two-photon absorption and two-photon luminescence in monolayer MoS_2 and WS_2 by defect repairing. *Opt. Express* **2019**, *27* (10), 13744−13753.
(71) Rosenberger, M. R.; Chuang, H. J.; McCreary, K. M.; Li, C. H.; Jonker, B. T. Electrical Characterization of Discrete Defects and

https://doi.org/10.1021/acsphotonics.1c00932
ACS Photonics XXXX, XXX, XXX−XXX

Impact of Defect Density on Photoluminescence in Monolayer WS2. *ACS Nano* **2018**, *12* (2), 1793−1800.
(72) Shaw, P. E.; Ruseckas, A.; Peet, J.; Bazan, G. C.; Samuel, I. D. W. Exciton−Exciton Annihilation in Mixed-Phase Polyfluorene Films. *Adv. Funct. Mater.* **2010**, *20* (1), 155−161.
(73) Mai, C.; Barrette, A.; Yu, Y.; Semenov, Y. G.; Kim, K. W.; Cao, L.; Gundogdu, K. Many-body effects in valleytronics: direct measurement of valley lifetimes in single-layer MoS_2. *Nano Lett.* **2014**, *14* (1), 202−206.
(74) Ugeda, M. M.; Bradley, A. J.; Shi, S. F.; da Jornada, F. H.; Zhang, Y.; Qiu, D. Y.; Ruan, W.; Mo, S. K.; Hussain, Z.; Shen, Z. X.; Wang, F.; Louie, S. G.; Crommie, M. F. Giant bandgap renormalization and excitonic effects in a monolayer transition metal dichalcogenide semiconductor. *Nat. Mater.* **2014**, *13* (12), 1091−1095.
(75) Linnros, J. Carrier lifetime measurements using free carrier absorption transients. I. Principle and injection dependence. *J. Appl. Phys.* **1998**, *84* (1), 275−283.
(76) Cui, Q.; Luo, Z.; Cui, Q.; Zhu, W.; Shou, H.; Wu, C.; Liu, Z.; Lin, Y.; Zhang, P.; Wei, S.; Yang, H.; Chen, S.; Pan, A.; Song, L. Robust and High Photoluminescence in WS_2 Monolayer through In Situ Defect Engineering. *Adv. Funct. Mater.* **2021**, 2105339.

https://doi.org/10.1021/acsphotonics.1c00932
ACS Photonics XXXX, XXX, XXX−XXX